Mean spherical approximation algorithm for multicomponent fluid mixtures with multi-screened Coulomb plus power series interactions

2003 J. Phys.: Condens. Matter 15 8213

(http://iopscience.iop.org/0953-8984/15/49/002)

INSTITUTE OF PHYSICS PUBLISHING JOURNAL OF PHYSICS: CONDENSED MATTER

J. Phys.: Condens. Matter **15** (2003) 8213–8233 PII: S0953-8984(03)69054-5

Mean spherical approximation algorithm for multicomponent fluid mixtures with multi-screened Coulomb plus power series interactions

M Yasutomi

Department of Physics and Earth Sciences, College of Science, University of the Ryukyus, Nishihara-Cho, Okinawa 903-0213, Japan

E-mail: g800002@lab.u-ryukyu.ac.jp

Received 15 September 2003
Published 25 November 2003
Online at stacks.iop.org/JPhysCM/15/8213

Abstract

An efficient algorithm is presented to find the Blum–Høye mean spherical approximation (MSA) solution for mixtures of hard-core fluids interacting through multi-screened Coulomb plus power series (multi-SCPPS) potentials. The solution for hard-sphere mixtures is used as an initial estimate of the variables. From this initial estimate only a few Newton–Raphson iterations are required to reach the final solution. The algorithm is also able to reflect correctly their molecular characteristics into the appropriate macroscopic behaviour. All MSA thermodynamic properties are presented analytically. Our analysis will be applicable to a large variety of fluid mixtures because any smooth, realistic isotropic potential can be well reproduced by the multi-SCPPS closure with arbitrary accuracy. Demonstrations of the power of the algorithm are made for two binary-component systems of Lennard-Jones particles. One is composed of particles with nearly the same sizes, while the other mixture with widely different sizes. We have studied their thermodynamic stabilities based on the compressibility and the isotherms of virial and energy equations of state, and further from microscopic viewpoints in connection with radial distribution functions. The present method is able to detect vapour–liquid transitions and perhaps liquid–glass transitions. The multi-SCPPS closure includes the multi-Yukawa closure as a special case.

1. Introduction

In our recent article [1], we have obtained an analytic solution of the Ornstein–Zernike (OZ) equation for multicomponent fluid mixtures interacting through multi-screened Coulomb plus power series (multi-SCPPS) potentials. The solution will be applicable to a large variety

of fluid mixtures and their thermodynamic properties will be derived analytically from the solution. As a few examples, we have shown an analytic structure factor for one-component, binary-component, and triple-component fluids of Lennard-Jones (LJ) particles [2, 3]. The immediate objective of the present work is to develop the multi-SCPPS-MSA method into a practical tool for the study of simple fluids and to provide a qualitative physical interpretation for its numerical results. The ultimate objective is to offer an alternative to the classical equation of state (EOS) for engineering applications involving fluid mixtures such as natural fluid including colloidal fluid. A subsequent paper will investigate the quantitative accuracy of the multi-SCPPS-MSA method by comparison to numerical simulations.

Blum and Høye (BH) [4] first formulated the MSA equations for mixtures of Yukawa fluids from a theoretical standpoint. Their analysis showed how to transform the problem into a system of nonlinear equations. For the simplest case (binary one-Yukawa mixtures), the first numerical results of the BH equations were obtained by Giunta *et al* [5]. They applied a slow, step-wise solution scheme which made their procedure rather cumbersome even for mixtures with very short-ranged interactions, for which the nonlinear equations become almost linear. Arrieta *et al* [6] provided a general, direct solution algorithm. Also, they extended the work by presenting an efficient, reliable solution algorithm for the most general case of their equations: multicomponent mixtures interacting through any number of Yukawa tails (multi-Yukawa closure) [7]. Their algorithm is quasianalytic in that its only numerical part, the solution of a system of nonlinear equations, takes just a few iterations to yield the unique stable solutions, whenever such solutions exist.

In the present work, we provide a solution algorithm for the most general case of the BH equations with multi-SCPPS closure which includes the multi-Yukawa closure as a special case. Our algorithm is sufficiently efficient and reliable: it takes just a few iterations to yield the unique stable solutions, whenever such solutions exist.

However, the reliability of the MSA is not guaranteed. It is well known that the MSA fails for significantly positive (repulsive) potentials. This can be best seen in the zero-density limit. In this case, positive potentials lead to negative radial distributions, a non-physical result [7].

On the other hand, the MSA is known to yield accurate thermodynamic properties for hard-core components with purely attractive soft interactions. This accuracy has been established for pure components by Henderson *et al* (one-Yukawa potential) [8], by Stell and Weis (hard-core attractive LJ) [9], by Konior and Jedrzejek (two-Yukawa fitted to the LJ interactions used by Stell and Weis) [10], and by Arrieta *et al* (three- and four-Yukawa fitted to two different truncated LJs) [7].

The multi-SCPPS closure is composed of a linear combination of several terms, called 'tails', which decrease exponentially with intermolecular distance. By the appropriate choice of the hard-core diameter and combination of coefficients, any smooth, realistic isotropic potential can be reproduced with arbitrary accuracy. The multi-SCPPS closure is obviously more flexible than the multi-Yukawa closure in fitting the closure to those potentials.

We demonstrate here the power of the algorithm for two binary-component LJ systems: one is composed of particles with nearly the same sizes, while the other with widely different sizes. Since exact closure for the OZ equation is not known and one has to use approximate closure for it, an arbitrary thermodynamic property calculated on the basis of one equation of state will not in general be the same if calculated on the basis of another one. For example, the pressure calculated from the virial equation will differ from the pressure found by means of the compressibility or energy equations. Therefore, we discuss here the thermodynamic stabilities of the mixtures based on the compressibility and the isotherms of virial and energy equations of state, and further study from microscopic standpoints in connection with particle distributions.

2. Baxter's factorized version of the OZ equation

Thermodynamic quantities of a fluid mixture will be derived from the total correlation functions (TCFs) $h_{ij}(r)$ or the radial distribution functions (RDFs) $g_{ij}(r) = 1+h_{ij}(r)$ between constituent particles i and j. These can be obtained by solving the OZ equation for the mixture written as

$$h_{ij}(r) = c_{ij}(r) + \sum_l \rho_l \int c_{il}(x) h_{lj}(|\mathbf{r} - \mathbf{x}|)\, \mathrm{d}\mathbf{x}, \tag{1}$$

where $c_{ij}(r)$ are the direct correlation functions (DCFs) and ρ_l represents the density of the component l in the mixture.

Let us consider here the interaction potential for the mixture of hard spheres of diameter σ_i with multi-screened Coulomb plus power series (multi-SCPPS) tails outside the core given by

$$\phi_{ij}(r) = \begin{cases} \infty & \text{for } r < \sigma_{ij}, \\ -k_\mathrm{B}T \displaystyle\sum_{n=1}^{N} \sum_{\tau=-1}^{L} K_{ij}^{(n,\tau)} z_n^{\tau+1} r^\tau \mathrm{e}^{-z_n r} & \text{for } r \geqslant \sigma_{ij}, \end{cases} \tag{2}$$

where $\sigma_{ij} = (\sigma_i + \sigma_j)/2$ (the additive hard-core assumption), k_B is the Boltzmann constant, T is a temperature, $K_{ij}^{(n,\tau)}$ and z_n are constants, and N and L are arbitrary integers.

In the mean spherical approximation (MSA) the closure for the OZ equation is given by the following two sets of equations:

$$h_{ij}(r) = -1 \qquad \text{for } r < \sigma_{ij}, \tag{3}$$

$$c_{ij}(r) = -\frac{\phi_{ij}(r)}{k_\mathrm{B}T} \qquad \text{for } r \geqslant \sigma_{ij}, \tag{4}$$

where equation (3) reflects the impenetrability to the hard cores and equation (4) accounts for the influence of the interaction potential outside the cores.

We will use Baxter's factorized version of the OZ equation (1) for mixtures as given by BH:

$$2\pi r h_{ij}(r) = -Q'_{ij}(r) + 2\pi \sum_l \rho_l \int_{\lambda_{jl}}^{\infty} (r-t) h_{il}(|r-t|) Q_{lj}(t)\, \mathrm{d}t, \tag{5}$$

$$2\pi r c_{ij}(r) = -Q'_{ij}(r) + \sum_l \rho_l \int_{\lambda_{lj}}^{\infty} Q_{jl}(t) Q'_{il}(r+t)\, \mathrm{d}t, \tag{6}$$

where $\lambda_{jl} = (\sigma_j - \sigma_l)/2$, and $Q_{ij}(r)$ are the factor correlation functions (FCFs), $Q'_{ij}(r)$ being their derivatives.

The functions $Q_{ij}(r)$ must have the following form:

$$Q_{ij}(r) = Q_{ij}^0(r) + \sum_{n=1}^{N} \sum_{\tau=-1}^{L} D_{ij}^{(\tau)}(z_n) z_n^{\tau+1} r^{\tau+1} \mathrm{e}^{-z_n r}, \tag{7}$$

where

$$Q_{ij}^0(r) = \tfrac{1}{2} A_j (r^2 - \sigma_{ij}^2) + B_j (r - \sigma_{ij}) + \sum_{n=1}^{N} \sum_{k=0}^{L+1} \sum_{\xi=0}^{k} \frac{z_n^{k-\xi} C_{ij}^{(k)}(z_n) k!}{(k-\xi)!} \times [r^{k-\xi} \mathrm{e}^{-z_n r} - \sigma_{ij}^{k-\xi} \mathrm{e}^{-z_n \sigma_{ij}}] \qquad \text{for } \lambda_{ji} \leqslant r < \sigma_{ij} \tag{8}$$

and $Q_{ij}^0(r) = 0$ otherwise [1]. The coefficients A_j, B_j and $C_{ij}^{(k)}(z_n)$ in equation (8) are given in appendix A.

The two sets of equations (5) and (6) can be led, respectively, to the following two sets of algebraic equations:

$$F_{1ij}^{(m)}(z_k) = \breve{A}_{ij}^{(m)}(z_k)A_j + \breve{B}_{ij}^{(m)}(z_k)B_j + \sum_{n=1}^{N}\sum_{\tau=0}^{L+1}\sum_{l}\breve{C}_{ilj}^{(m,\tau)}(z_k,z_n)\breve{C}_{lj}^{(\tau)}(z_n) + \sum_{n=1}^{N}\sum_{\tau=-1}^{L}\sum_{l}\breve{D}_{ilj}^{(m,\tau)}(z_k,z_n)\mathcal{D}_{lj}^{(\tau)}(z_n)K_{n_1n_2}^{(n,\tau)} - \exp[\mathcal{G}_{ij}^{(m+1)}(z_k)] = 0, \tag{9}$$

and

$$\begin{aligned} F_{2ij}^{(m)}(z_n) = {} & -\frac{K_{ij}^{(n,m-1)}}{K_{n_1n_2}^{(n,m-1)}} + \sum_{l}\mathcal{D}_{il}^{(m-1)}(z_n)[\delta_{jl} - \rho_l\tilde{Q}_{jl}^{(0)}(\mathrm{i}z_n)] \\ & - (m+1)\sum_{l}\mathcal{D}_{il}^{(m)}(z_n)\frac{K_{n_1n_2}^{(n,m)}}{K_{n_1n_2}^{(n,m-1)}}[\delta_{jl} + z_n\rho_l\tilde{Q}_{jl}^{(1)}(\mathrm{i}z_n) - \rho_l\tilde{Q}_{jl}^{(0)}(\mathrm{i}z_n)] \\ & + \sum_{\tau=m+1}^{L}\sum_{l}\mathcal{D}_{il}^{(\tau)}(z_n)\frac{K_{n_1n_2}^{(n,\tau)}}{K_{n_1n_2}^{(n,m-1)}}\frac{z_n^\tau}{z_n^m}\rho_l \\ & \times [(\tau+1)C_{\tau-m}^{\tau}\tilde{Q}_{jl}^{(\tau-m)}(\mathrm{i}z_n) - C_{\tau+1-m}^{\tau+1}z_n\tilde{Q}_{jl}^{(\tau+1-m)}(\mathrm{i}z_n)] = 0, \end{aligned} \tag{10}$$

where $m = 0, 1, 2, \ldots,$ and $L+1$, and the coefficients $\breve{A}_{ij}^{(m)}(z_k)$, $\breve{B}_{ij}^{(m)}(z_k)$, $\breve{C}_{ilj}^{(m,\tau)}(z_k,z_n)$, $\breve{D}_{ilj}^{(m,\tau)}(z_k,z_n)$ and functions $\tilde{Q}_{lj}^{(m)}(\mathrm{i}s)$ are given in appendix B.

All quantities presented above are determined by the two sets of unknowns $\{\mathcal{D}_{il}^{(\tau)}(z_n)\}$ and $\{\mathcal{G}_{ij}^{(\tau)}(z_k)\}$. These two sets of unknowns are obtained by solving the two sets of algebraic equations (9) and (10).

3. Solution method

A system of equations (9) and (10) is solved using the Newton–Raphson technique, with the partial derivatives evaluated analytically. This iterative technique provides a fast and reliable convergence to the final solution. Since $\mathcal{G}_{ij}^{(m)}(z_k) = \mathcal{G}_{ji}^{(m)}(z_k)$ for all m and k, one can reduce the number of equations (9) by $NI(I-1)(L+2)/2$ where I is the number of species of particles in the fluid mixture. However, a simplification of the system is possible only through the use of a symbolic manipulation program and leads to a very considerable complication of the remaining equations. In the process, the symmetric structure of the equations (which facilitates their evaluation) is likely to be lost, and their convergence properties may be altered. In the meantime, equations (10) show that when one of $K_{ij}^{(n,m-1)}$ is zero an equation $F_{2ij}^{(m)}(z_n) = 0$ becomes equivalently zero. It makes one of the unknowns $\mathcal{D}_{il}^{(m)}(z_n)$ zero. Therefore, unknowns $\mathcal{D}_{il}^{(m)}(z_n)$ are reduced by the number N_0 of parameters $K_{ij}^{(n,m)}$ with a zero value. Thus, the system is finally reduced to $[2NI^2(L+2) - N_0]$ equations.

As a measure of the error for any set of values of the variables, the following norm of the deviations is used:

$$\Omega = \sqrt{\frac{1}{2NI^2(L+2) - N_0}\sum_{n=1}^{N}\sum_{i,j=1}^{I}\sum_{m=0}^{L+1}\left\{\left[\frac{F_{1ij}^{(m)}(z_n)}{F_{1ij}^{0(m)}(z_n)}\right]^2 + [F_{2ij}^{(m)}(z_n)]^2\right\}}, \tag{11}$$

where the normalization constants $F_{1ij}^{0(m)}(z_n)$ are given in equation (20) below.

A tolerance $\Omega \leqslant 10^{-6}$ is sufficiently small to determine uniquely the first six significant digits for all thermodynamic properties. The above norm of the error is tested at every Newton–Raphson iteration to avoid overshooting.

An essential part in any iterative method is the initial estimation of the solution. The solution for hard-sphere mixtures can be used as an initial estimate which is given by

$$\mathcal{D}_{ij}^{(m-1)}(z_\eta) = \breve{C}_{ij}^{(m)}(z_\eta) = 0, \tag{12}$$

and

$$\mathcal{G}_{ij}^{(m)}(z_\eta) = \ln\left[\frac{z_\eta^2 \mathrm{e}^{z_\eta\sigma_{ij}}}{2\pi\sqrt{\rho_i\rho_j}}\{\hat{\Gamma}^{0(m)}(z_\eta)\}_{ij}\right] \tag{13}$$

for all i, j, η and m. The matrices $\hat{\Gamma}^{0(m)}(z_\eta)$ are given by the following asymptotic relations:

$$\hat{\Gamma}^{0(1)}(z_\eta) = \hat{\Lambda}^{0(0)}(z_\eta)(\hat{Q}^{0(0,0)}(\mathrm{i}z_\eta))^{-1}, \tag{14}$$

and

$$\hat{\Gamma}^{0(m+1)}(z_\eta) = \left[\hat{\Lambda}^{0(m)}(z_\eta) - \sum_{\xi=0}^{m-1}\hat{\Gamma}^{0(\xi+1)}(z_\eta)\hat{Q}^{0(m,\xi)}(\mathrm{i}z_\eta)\right](\hat{Q}^{0(0,0)}(\mathrm{i}z_\eta))^{-1}. \tag{15}$$

The matrices $\hat{\Lambda}^{0(m)}(z_\eta)$ and $\hat{Q}^{0(m,\xi)}(\mathrm{i}z_\eta)$ are defined as

$$\{\hat{\Lambda}^{0(m)}(z_\eta)\}_{ij} = \frac{(\rho_i\rho_j)^{1/2}}{z_\eta}\{A_j^0\chi^{(m+1)}(\sigma_{ij}, z_\eta) + B_j^0\chi^{(m)}(\sigma_{ij}, z_\eta)\} \tag{16}$$

and

$$\{\hat{Q}^{0(m,\xi)}(\mathrm{i}z_\eta)\}_{lj} = \delta_{lj}\delta_{m\xi} - C_\xi^m(\rho_l\rho_j)^{1/2}\tilde{Q}_{lj}^{0(m-\xi)}(\mathrm{i}z_\eta), \tag{17}$$

where

$$A_j^0 = \frac{2\pi}{\Delta}\left(1 + \frac{\pi\zeta_2}{2\Delta}\sigma_j\right), \qquad B_j^0 = -\frac{\zeta_2}{2}\left(\frac{\pi}{\Delta}\right)^2\sigma_j^2 \tag{18}$$

and

$$\mathrm{e}^{-z_\eta\lambda_{lj}}\tilde{Q}_{lj}^{0(m)}(\mathrm{i}z_\eta) = \tfrac{1}{2}A_j^0\Phi_{lj}^{(m+2,m)}(z_\eta, 0) + B_j^0\Phi_{lj}^{(m+1,m)}(z_\eta, 0). \tag{19}$$

The normalization constants $F_{1ij}^{0(m)}(z_n)$ in equation (11) are defined by

$$F_{1ij}^{0(m)}(z_k) = \breve{A}_{ij}^{0(m)}(z_k)A_j^0 + \breve{B}_{ij}^{0(m)}(z_k)B_j^0, \tag{20}$$

where

$$\breve{A}_{ij}^{0(m)}(z_k) = \frac{z_k\mathrm{e}^{z_k\sigma_{ij}}}{2\pi}\chi^{(m+1)}(\sigma_{ij}, z_k) \tag{21}$$

and

$$\breve{B}_{ij}^{0(m)}(z_k) = \frac{z_k\mathrm{e}^{z_k\sigma_{ij}}}{2\pi}\chi^{(m)}(\sigma_{ij}, z_k). \tag{22}$$

In most cases, only a few iterations are needed to reach the final solution. The correctness of the present algorithm was verified by the method which will be presented in the next section.

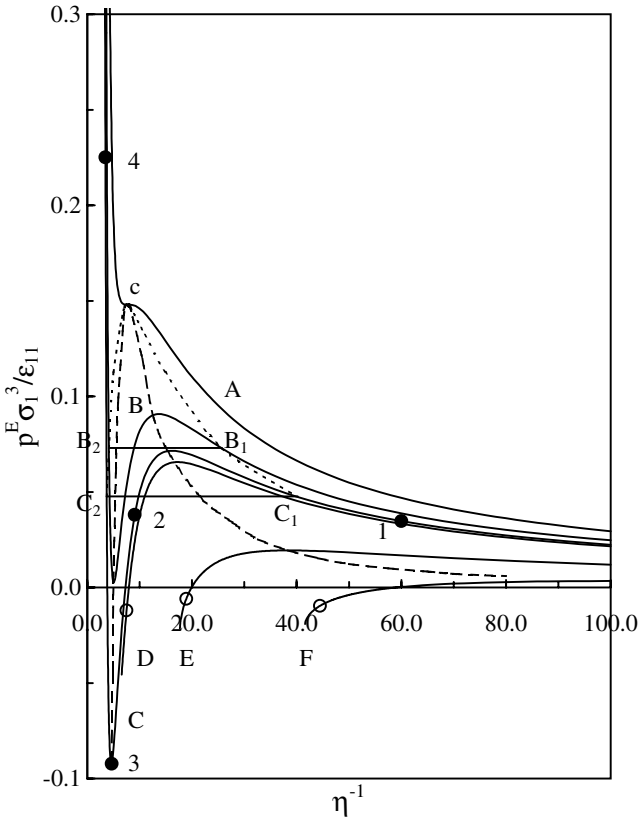

Figure 1. Isotherms of energy pressure p^{E} for model 1. Solid curves labelled A, B, C, D, E and F show the isotherms for $T^*_{\mathrm{crit}} = 2.1322$, $T^*_{\mathrm{B}} = 1.8182$, $T^*_{\mathrm{C}} = 1.6667$, $T^*_{\mathrm{D}} = 1.6129$, $T^*_{\mathrm{E}} = 1$ and $T^*_{\mathrm{F}} = 0.5$, respectively. The dashed curve is a spinodal, c is the critical point, while the dotted curve is a binodal. Horizontal lines B_1–B_2 and C_1–C_2 are Maxwell constructions for isotherms B and C, respectively. Open circles on the isotherms D, E and F are the boundary states beyond which distribution functions $g_{ij}(r)$ diverge at infinite r.

4. Thermodynamic properties

4.1. Static structure factors and radial distribution functions

The Fourier-transformed OZ equation is given by

$$\sum_l [\delta_{il} - \rho_l \tilde{c}_{il}(k)]\tilde{h}_{lj}(k) = \tilde{c}_{ij}(k), \tag{23}$$

where

$$\tilde{h}_{ij}(k) \equiv \int \mathrm{d}\mathbf{r}\, \mathrm{e}^{\mathrm{i}\mathbf{k}\cdot\mathbf{r}} h_{ij}(r) = \frac{4\pi}{k}\int_0^\infty \mathrm{d}r\, r h_{ij}(r)\sin(kr) \tag{24}$$

and

$$\tilde{c}_{ij}(k) \equiv \int \mathrm{d}\mathbf{r}\, \mathrm{e}^{\mathrm{i}\mathbf{k}\cdot\mathbf{r}} c_{ij}(r) = \frac{4\pi}{k}\int_0^\infty \mathrm{d}r\, r c_{ij}(r)\sin(kr). \tag{25}$$

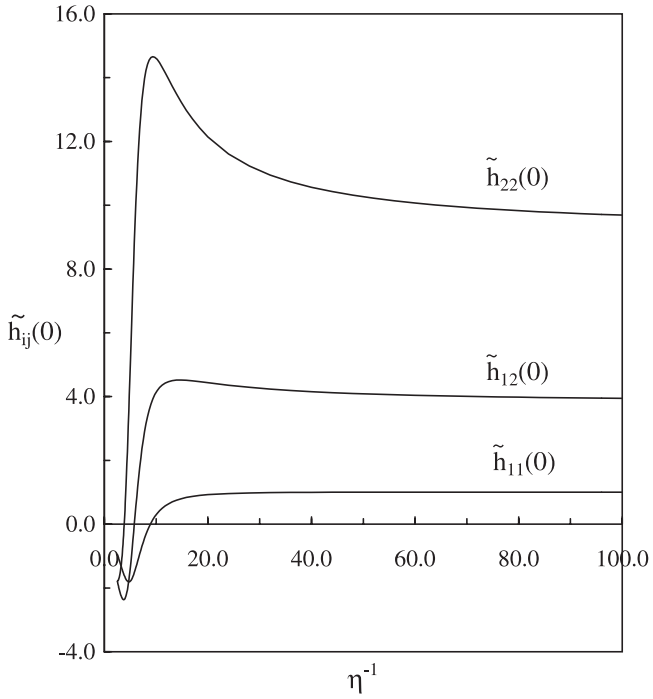

Figure 2. FTCFs $\tilde{h}_{ij}(0)$ as a function of η^{-1} for the reduced critical temperature T^*_{crit}.

In the absence of infinitely ranged correlations the Fourier-transformed DCFs $\tilde{c}_{ij}(k)$ can be factorized and given by

$$\tilde{c}_{ij}(k) = \tilde{Q}^{(0)}_{ij}(k) + \tilde{Q}^{(0)}_{ji}(-k) - \sum_l \rho_l \tilde{Q}^{(0)}_{il}(k)\tilde{Q}^{(0)}_{jl}(-k). \tag{26}$$

The Fourier-transformed total correlation functions (FTCFs) $\tilde{h}_{ij}(k)$ are obtained by solving the linear equation (23) with (26).

The partial and total structure factors $S_{ij}(k)$ and $S(k)$ are given by

$$S_{ij}(k) = \delta_{ij} + \rho(c_i c_j)^{1/2}\tilde{h}_{ij}(k) \tag{27}$$

and

$$S(k) = 1 + \sum_{ij} \rho c_i c_j \tilde{h}_{ij}(k) \tag{28}$$

where $c_j = \rho_j/\rho$ (ρ is the total number density).

The RDFs can be obtained from equation (5) with (7) and (8). The following is a stepwise algorithm for their calculation. Let us define

$$\bar{g}_{il}(m) = g_{il}(\sigma_{il} + m\Delta r) \qquad \text{and} \qquad \bar{Q}_{lj}(m) = Q_{lj}(\lambda_{jl} + m\Delta r), \tag{29}$$

where Δr is the step size and m is the number of steps. For each step $m \geqslant 1$, $\bar{g}_{ij}(m)$ is obtained by solving the linear system

$$2\pi \sum_l \{\delta_{jl}(\sigma_{il} + m\Delta r) - \tfrac{1}{2}\rho_l \Delta r\, \bar{Q}_{lj}(0)(\sigma_{il} + m\Delta r)\}\bar{g}_{il}(m)$$

$$= A_j(\sigma_{ij} + m\Delta r) + B_j - \sum_{n=1} \mathrm{e}^{-z_n(\sigma_{ij}+m\Delta r)} z_n \sum_{k=0}^{L+1} z_n^k (\sigma_{ij} + m\Delta r)^k C^{(k)}_{ij}(z_n)$$

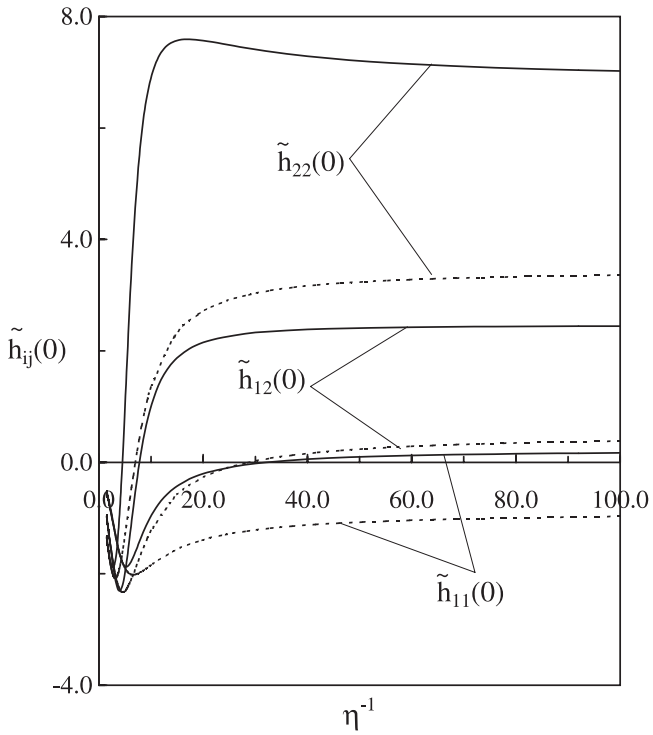

Figure 3. The same as figure 2 but for $T^* = 2.5$ (solid curves) and 3.33 (dotted curves).

$$+\pi\Delta r\sum_l \rho_l\left\{\bar{Q}_{lj}(m)\sigma_{il}\bar{g}_{il}(0)+2\sum_{n=1}^{m-1}\bar{Q}_{lj}(m-n)(\sigma_{il}+n\Delta r)\bar{g}_{il}(n)\right\}. \quad (30)$$

A step size Δr should be so small that significant differences do not appear between $\bar{g}_{il}(m)$ and $\bar{g}_{li}(m)$. The contact values are given by

$$2\pi\sigma_{ij}g_{ij}(\sigma_{ij}) = A_j\sigma_{ij} + B_j - \sum_{n=1} e^{-z_n\sigma_{ij}} z_n \sum_{k=0}^{L+1}(z_n\sigma_{ij})^k C_{ij}^{(k)}(z_n). \quad (31)$$

The corresponding hard-sphere quantity is

$$2\pi\sigma_{ij}g_{ij}^0(\sigma_{ij}) = A_j^0\sigma_{ij} + B_j^0. \quad (32)$$

4.2. Thermodynamic quantities

From the correlation parameters, thermodynamic properties can be calculated directly. Configurational energy U^c per molecule is given by

$$\frac{U^c}{\mathcal{N}} = -k_B T\sum_{ij} c_i \sum_{n=1}^{N}\sum_{\tau=-1}^{L} K_{ij}^{(n,\tau)} z_n \gamma_{ij}^{(\tau+2)}(z_n) \quad (33)$$

where $\mathcal{N}$ is the total number of molecules in the system. Inverse isothermal compressibility is given by

$$\chi^{-1} = \frac{1}{k_B T}\left(\frac{\partial p}{\partial\rho}\right)_T = 1 - \rho\sum_{ij} c_i c_j \tilde{c}_{ij}(0) = \sum_j c_j\left(\frac{A_j}{2\pi}\right)^2 \quad (34)$$

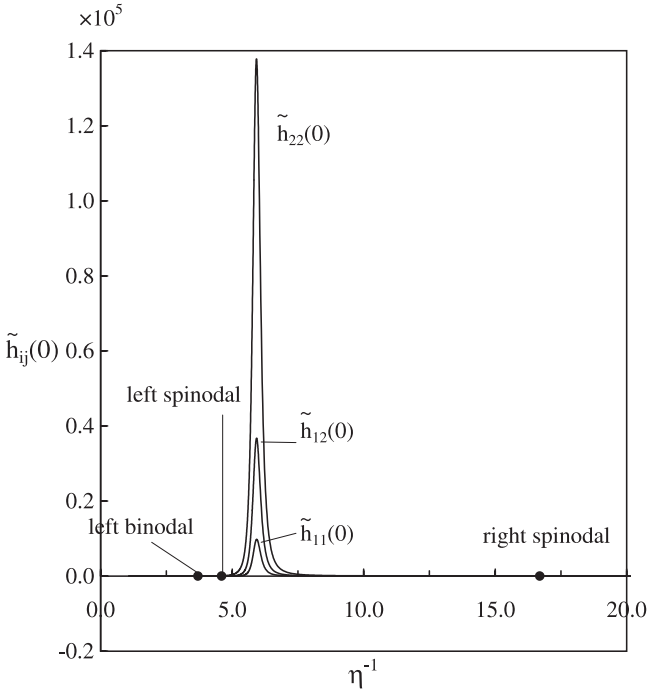

Figure 4. The same as figure 2 but for T_C^*.

and the corresponding hard-sphere quantity is

$$\chi_0^{-1} = \sum_j c_j \left(\frac{A_j^0}{2\pi}\right)^2. \tag{35}$$

The virial pressure, p^V, is obtained through

$$\frac{p^V}{\rho k_B T} = 1 + \frac{2\pi\rho}{3} \sum_{ij} c_i c_j \sigma_{ij}^3 g_{ij}(\sigma_{ij}) + J, \tag{36}$$

where

$$J = \tfrac{1}{3} \sum_{ij} c_i \sum_{n=1}^{N} \sum_{\tau=-1}^{L} K_{ij}^{(n,\tau)} z_n [\tau \gamma_{ij}^{(\tau+2)}(z_n) - \gamma_{ij}^{(\tau+3)}(z_n)]. \tag{37}$$

We have already obtained $\gamma_{ij}^{(\tau)}(z_n)$ for $\tau \leqslant L+2$ by solving equations (9) and (10), while the computation of $\gamma_{ij}^{(L+3)}(z_n)$ is presented in appendix C.

In most applications the equation of state obtained by differentiating the energy equation is more accurate than those obtained from either the pressure equation or the compressibility [11]. According to the method of Høye and Stell [12] the incremental energy pressure Δp^E is found from

$$\frac{\Delta p^E}{\rho k_B T} = \frac{\pi}{3} \rho \sum_{ij} c_i c_j \sigma_{ij}^3 ([g_{ij}(\sigma_{ij})]^2 - [g_{ij}^0(\sigma_{ij})]^2) + J. \tag{38}$$

The incremental Helmholtz free energy is yielded by

$$\frac{\Delta A}{\mathcal{N} k_B T} = \frac{U^c}{\mathcal{N} k_B T} - \frac{\Delta p^E}{\rho k_B T} + \frac{1}{2}(\chi^{-1} - \chi_0^{-1}). \tag{39}$$

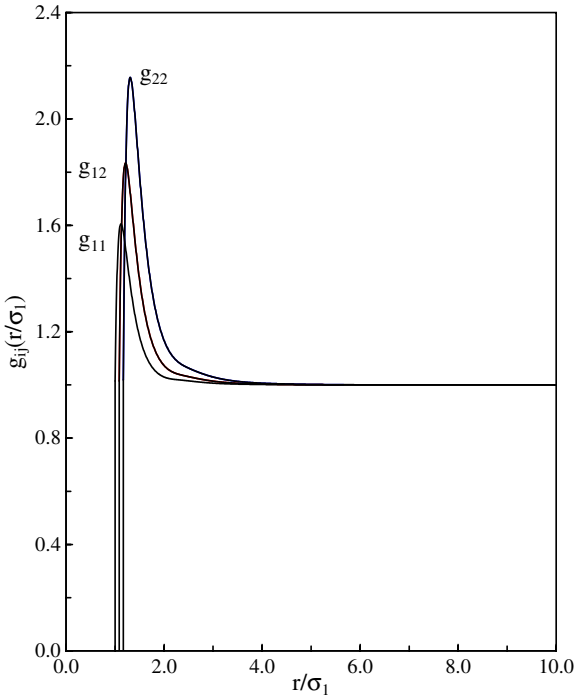

Figure 5. RDF $g_{ij}(r)$ for characteristic thermodynamic state 1 marked by the closed circle on isotherm C in figure 1.

As mentioned in the previous section, the correctness of the MSA solutions yielded by this multi-SCPPS algorithm can be verified by comparing the values of $\gamma_{ij}^{(L+3)}(z_n)$ calculated by the method presented in appendix C with those calculated by direct numerical integration using relations (A.10) in appendix A.

5. Applications to Lennard-Jones fluid mixtures

In this section we demonstrate the power of the multi-SCPPS-MSA algorithm for two binary-component LJ systems: one is composed of particles with nearly the same sizes, while the other with widely different sizes.

5.1. Fitting procedure of the SCPPS closure to the Lennard-Jones potentials

Let us consider here fluid mixtures with LJ interactions which are given by

$$\phi_{ij}^{\mathrm{LJ}}(r) = 4\epsilon_{ij}\left[\left(\frac{\sigma_{ij}}{r}\right)^{12} - \left(\frac{\sigma_{ij}}{r}\right)^{6}\right]. \tag{40}$$

For any values of LJ parameters ϵ_{ij} and σ_{ij}, the potentials $\phi_{ij}^{\mathrm{LJ}}(r)$ can be reproduced with arbitrary accuracy by the single-SCPPS closure, all of whose parameters are obtained from only one z and $(L+2)$ of a_τ defined by

$$z = z_{n_{ij}}\sigma_{ij}, \qquad a_\tau = -\frac{k_{\mathrm{B}}T}{\epsilon_{ij}}\frac{K_{ij}^{(n_{ij},\tau)}}{\sigma_{ij}}z^{\tau+1}. \tag{41}$$

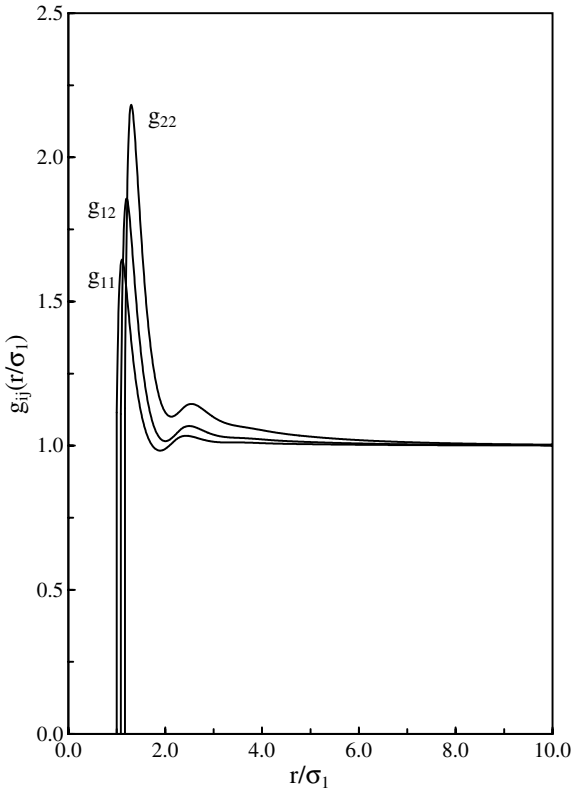

Figure 6. The same as figure 5 but for characteristic state 2.

The fitting parameters z and a_τ are adjusted, using the Levenberg–Marquardt technique [13], to fit the single-SCPPS potential $\phi(x)$ to an LJ potential $\phi^{\mathrm{LJ}}(x)$ as follows:

$$\phi^{\mathrm{LJ}}(x) \equiv 4\left(\frac{1}{x^{12}} - \frac{1}{x^6}\right) = \phi(x) \equiv \sum_{\tau=-1}^{L} a_\tau x^\tau \mathrm{e}^{-zx}. \tag{42}$$

As a measure of the error for the values of the fitting parameters, the following norm of the deviations is used:

$$\Omega_\phi = \sqrt{\frac{1}{K}\sum_{k=1}^{K}[\phi(x_k) - \phi^{\mathrm{LJ}}(x_k)]^2}. \tag{43}$$

All fitting points x_k are spaced with an even step Δs along the curve of $\phi^{\mathrm{LJ}}(x)$ as follows:

$$x_{k+1} - x_k = \frac{\Delta s}{\sqrt{1 + \phi'^{\mathrm{LJ}}(x_k)^2}}. \tag{44}$$

Under the deviation norm $\Omega_\phi = 10^{-4}$ with $K = 200$ fitting points between $1 \leqslant x \leqslant 5$, the fitting parameters obtained are $z = 5.0$ and $a_\tau = 3.918\,470 \times 10^5$, $-2.008\,409 \times 10^6$, $4.566\,117 \times 10^6$, $-6.027\,436 \times 10^6$, $5.077\,946 \times 10^6$, $-2.826\,468 \times 10^6$, $1.038\,145 \times 10^6$, $-2.424\,914 \times 10^5$, $3.269\,131 \times 10^4$ and $-1.941\,919 \times 10^3$ for $\tau = -1, 0, 1, 2, \ldots$, and $L = 8$, respectively.

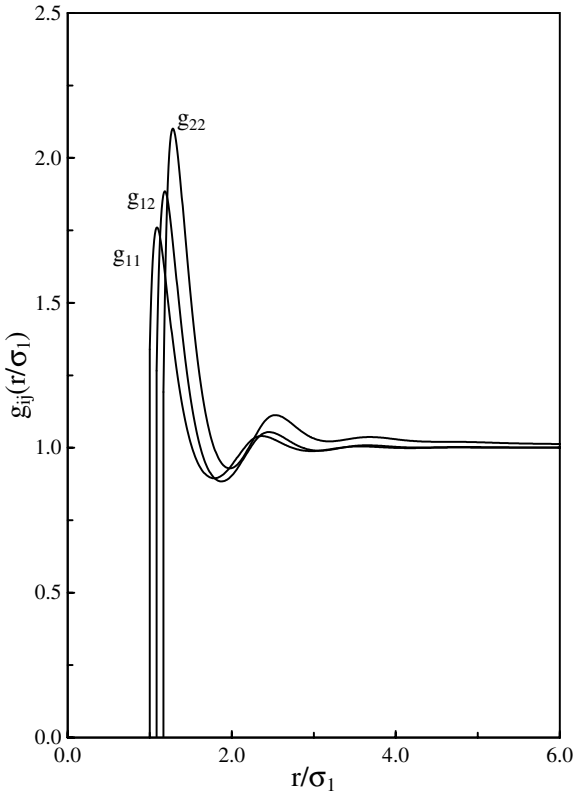

Figure 7. The same as figure 5 but for characteristic state 3.

This work provides numerical results for two specific binary mixtures, designated as M1 and M2. The first mixture M1 has model parameters chosen to resemble an argon–xenon mixture: $\sigma_2/\sigma_1 = 1.167$, $\epsilon_2/\epsilon_1 = 1.919$, $\epsilon_{12} = \sqrt{\epsilon_1\epsilon_2}$, and $c_1 = c_2$. On the other hand, the model parameters of the second mixture M2 are artificially set as $\sigma_2/\sigma_1 = 5$, $\epsilon_2/\epsilon_1 = 2$, $\epsilon_{12} = \sqrt{\epsilon_1\epsilon_2}$ and $c_1 = c_2$.

For the binary LJ mixtures, the symbols n_{ij} in equation (41) can be expressed as $n_{11} = 1$, $n_{12} = n_{21} = 2$ and $n_{22} = 3$. In this case, the nonzero parameters z_n ($n = 1$, 2 and 3), $K_{11}^{(1,\tau)}$, $K_{12}^{(2,\tau)} = K_{21}^{(2,\tau)}$ and $K_{22}^{(3,\tau)}$ are given by equations (41). The rest of the parameters $K_{ij}^{(n,\tau)}$ are all zero and we can see from equation (10) that $F_{211}^{(\tau)}(z_3)$, $F_{212}^{(\tau)}(z_3)$, $F_{221}^{(\tau)}(z_1)$ and $F_{222}^{(\tau)}(z_1)$ are equivalently zero and $\mathcal{D}_{11}^{(\tau)}(z_3) = \mathcal{D}_{12}^{(\tau)}(z_3) = \mathcal{D}_{21}^{(\tau)}(z_1) = \mathcal{D}_{22}^{(\tau)}(z_1) = 0$ for all τ. Thus, the parameters N, I, L and N_0 in equation (11) are given as 3, 2, 8 and 40, respectively. Also, the normalization constants $K_{n_1n_2}^{(n,\tau)}$ in equation (10) are set as $K_{n_1n_2}^{(1,\tau)} = K_{11}^{(1,\tau)}$, $K_{n_1n_2}^{(2,\tau)} = K_{12}^{(2,\tau)}$ and $K_{n_1n_2}^{(3,\tau)} = K_{22}^{(3,\tau)}$.

5.2. Thermodynamic properties of mixture M1

The isotherms of energy pressure p^{E} are shown in figure 1 by solid curves. The isotherm at critical temperature $T_{\mathrm{crit}}^*(= k_{\mathrm{B}}T_{\mathrm{crit}}/\epsilon_{11}) = 2.1322$ shown by curve A has a critical point c where $(\partial p^{\mathrm{E}}/\partial\eta^{-1})_{\mathrm{T}} = (\partial^2 p^{\mathrm{E}}/\partial(\eta^{-1})^2)_{\mathrm{T}} = 0$. At temperatures above T_{crit}^* the isotherms are single-valued decreasing functions of η^{-1}, but below T_{crit}^* the isotherms exhibit so-called van

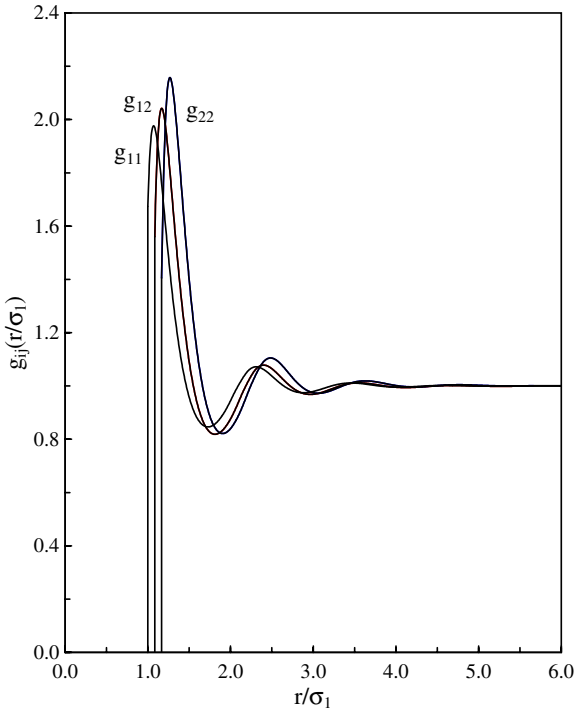

Figure 8. The same as figure 5 but for characteristic state 4.

der Waals loops (curve B at $T^*_B = 1.8182$ and curve C at $T^*_C = 1.6667$): at low and high densities p^E decreases with η^{-1}, but in the intermediate-density range p^E has both a maximum and a minimum, separated by a region where p^E is an increasing function of η^{-1}. This region corresponds to thermodynamically unstable states, because the isothermal compressibility $(\partial p^E/\partial \eta^{-1})_T$ is positive. The unstable states can be eliminated by replacing the loops by horizontal segments (line B_1–B_2 for curve B and line C_1–C_2 for curve C) through the Maxwell equal-area construction in the p^E–η^{-1} plane [14, 15]. The dashed curve shows a spinodal curve which is the locus of points where $(\partial p^E/\partial \eta^{-1})_T = 0$. The dotted curve is a binodal curve which shows the locus of coexistence points satisfying the Maxwell construction. All thermodynamic states falling between the spinodal and binodal curves are metastable, but can be reached experimentally if sufficient care is taken [16]. Below the temperature T^*_C the stable branch of the isotherms in the high-density range disappears as shown by curves D, E and F at $T^*_D = 1.6129$, $T^*_E = 1$ and $T^*_F = 0.5$, respectively.

Let us study the isotherms in connection with the FTCFs, $\tilde{h}_{ij}(0)$, which are closely related to the phase behaviour of the system. Figure 2 represents the variation of $\tilde{h}_{ij}(0)$ with η^{-1} at T^*_{crit}. The FTCF $\tilde{h}_{22}(0)$ has a small peak at $\eta^{-1} = 9.36$ which is a little shifted from the critical point, $\eta^{-1} = 7.5$. Such a peak becomes smaller and disappears with increasing temperature as shown in figure 3 at $T^* = 2.5$ (solid curves) and 3.33 (dotted curves). On the other hand, it sharpens drastically with decreasing temperature: the peak values of $\tilde{h}_{11}(0)$, $\tilde{h}_{12}(0)$ and $\tilde{h}_{22}(0)$ are 9.8×10^3, 3.7×10^4 and 1.4×10^5, respectively, at $T^* = T^*_C$ (see figure 4), and 1.6×10^8, 2.9×10^8 and 5.1×10^8, respectively, at $T^* = T^*_F$. Every unstable branch of the isotherm at different temperature also has such a sharpened peak of $\tilde{h}_{ij}(0)$ at some thermodynamic state on the branch.

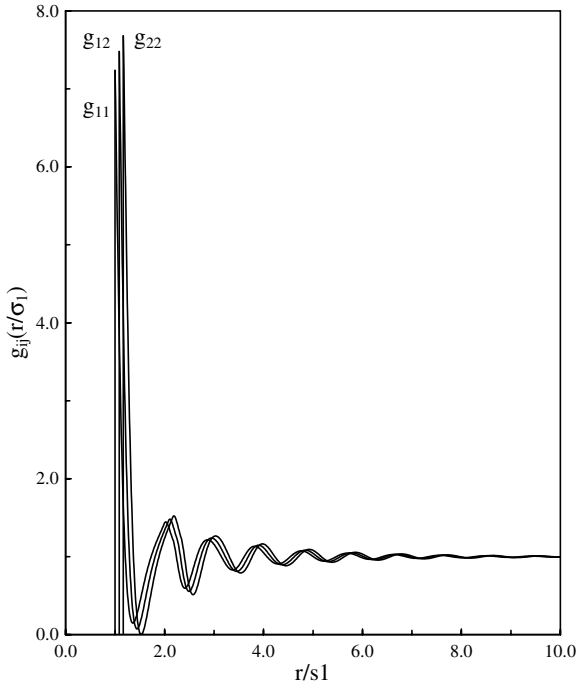

Figure 9. The same as figure 5 but for the state of $p^{\mathrm{E}}\sigma_1^3/\epsilon_{11} = 110.8$ and $\eta = 0.598$ on isotherm C.

We next study the isotherms from the viewpoint of particle distributions. In this sense, we can consider curve C as a representative of isotherms at temperatures between T^*_{crit} and T^*_{C}. The distribution functions $g_{ij}(r)$ are presented in figures 5–8, respectively, for the characteristic states at 1–4 which are shown by closed circles on isotherm C in figure 1. Figure 5 shows simple behaviours (one peak) of $g_{ij}(r)$ which are characteristic of stable gas states. As the thermodynamic state moves from the stable gas branch to the stable liquid branch via the unstable branch along isotherm C, the number of peaks of $g_{ij}(r)$ increases and simultaneously their oscillations are amplified, and thus the first depression of $g_{22}(r)$ reaches zero value at the state of $p^{\mathrm{E}}\sigma_1^3/\epsilon_{11} = 110.8$ and $\eta = 0.598$ as shown in figure 9. Beyond this state the first depressions of $g_{ij}(r)$ become negative. Arrieta *et al* [7] speculated that the limit signals the end of the fluid range; beyond, only amorphous (glassy) or ordered (crystalline) solids can be found. The limit itself has been interpreted as the transition from metastable fluid to metastable glass.

On the other hand the Hansen–Verlet freezing criterion [17] states that crystallization of simple liquids occurs when the structure factor $S(k)$ increases to a value of 2.85 at some k_0. Sarkisov [18] proposed another semiempirical microscopic structural criterion of melting, and showed that both the Hansen–Verlet criterion for freezing and the Sarkisov criterion for melting outline the freezing–melting area very satisfactorily. We will discuss the liquid-crystal phase diagram in a subsequent paper.

Now, let us study the behaviours of the distribution functions for thermodynamic states on the isotherms at a temperature lower than T^*_{C}. Their qualitative behaviours are the same as mentioned before for larger η^{-1}, but the distribution functions diverge at infinite r in the lower region of η^{-1}. As a representative of the latter case, we have shown the behaviours of $g_{ij}(r)$

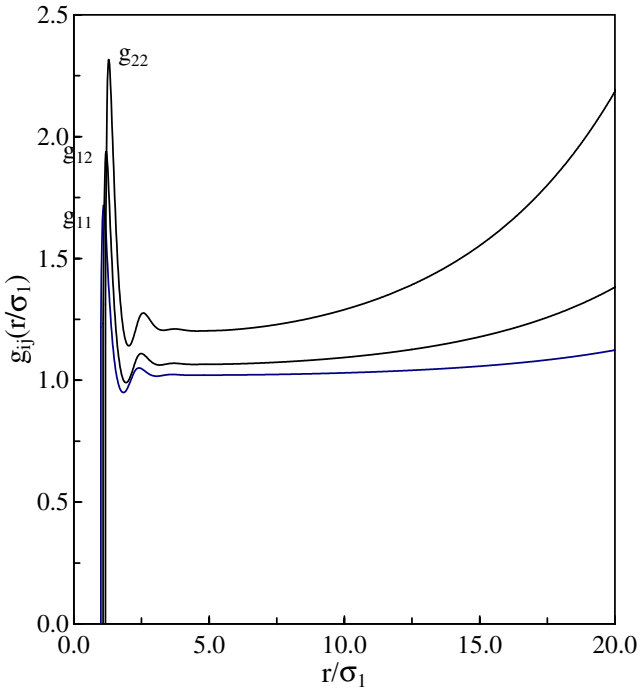

Figure 10. RDF $g_{ij}(r)$ for the left-hand edge of isotherm D in figure 1.

in figure 10 for the thermodynamic state of the left-hand edge of isotherm D in figure 1. The boundaries between the divergence and convergence of distribution functions at infinite r are located at $\eta^{-1} = 7.5$, 18.9 and 44.5, respectively, for isotherms D, E and F as shown by open circles in figure 1.

Finally, we study the discrepancies among the results obtained from the compressibility χ given by equation (34) and the isotherms of virial pressure p^{V} given by equation (36) and energy pressure p^{E} given by equation (38). First, we have shown the isotherms of virial pressure p^{V} in figure 11, where the letters A to F attached to the curves have the same meanings as in figure 1. It is well known that the isotherms of p^{E} and p^{V} coincide well in the high-temperature and low-density region. We also found that both the isotherms coincide well in the low-temperature range by comparing the isotherms of E and F in figure 11 with those in figure 1, respectively. On the other hand, the differences between the isotherms of p^{E} and p^{V} are appreciable in the intermediate-temperature range. Next, we present the behaviours of the inverse isothermal compressibility χ^{-1} in figure 12. The letters attached to the curves have the same meanings as in figure 1. Since negative, zero or nearly zero values of χ^{-1} are never found in figure 12, we can never detect from the compressibility equation any unstable thermodynamic states as found in the isotherms of p^{E} and p^{V}.

5.3. Thermodynamic properties of mixture M2

In this subsection, we study the thermodynamic properties of mixture M2 which is composed of particles with widely different sizes ($\sigma_2/\sigma_1 = 5$). The isotherms of energy pressure p^{E} are shown in figure 13 and those of virial pressure p^{V} are presented in figure 14. In both figures, the letters A, B, C, D and E attached to solid curves show the reduced temperatures $T^*_{\mathrm{A}} = 2.427$,

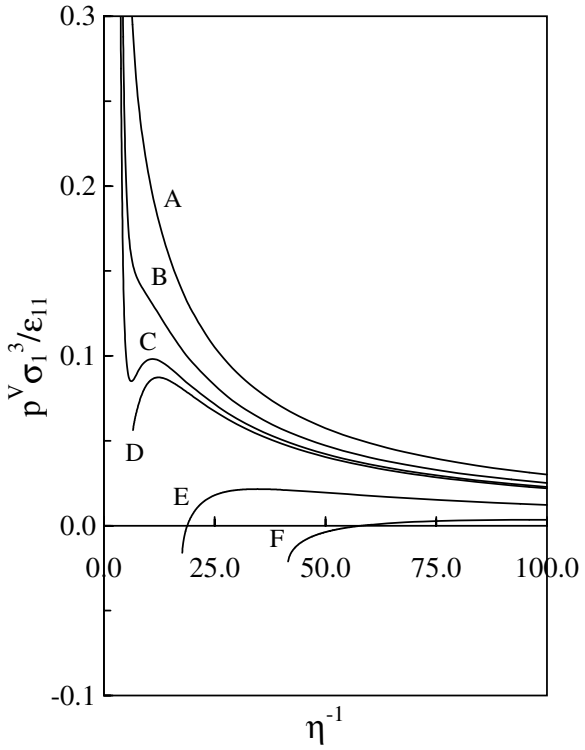

Figure 11. The same as figure 1 but for the virial pressure p^{V}.

$T_{\mathrm{B}}^* = 2.041$, $T_{\mathrm{C}}^* = 2.0$, $T_{\mathrm{D}}^* = 1.667$ and $T_{\mathrm{E}}^* = 1.0$, respectively. The temperature T_{A}^* is a critical one for the isotherm of p^{E}. In figure 13, the dashed curve shows a spinodal curve and the dotted curve is a binodal curve. The physical properties of mixture M2 are qualitatively not so different from those of mixture M1 macroscopically and microscopically (from the viewpoint of particle distributions though not shown here) in the parameter range considered here.

6. Conclusions

We have presented an efficient numerical algorithm for solving the BH MSA equations for multicomponent fluid mixtures interacting through multi-SCPPS potentials. Analytic expressions are presented for the calculation of all MSA thermodynamic properties. The only numerical part of the algorithm is the solution of a system of nonlinear equations. This algorithm is sufficiently fast and is reliable in that it converges to the physical solution, if it exists. It offers sufficient flexibility and opens access to systems with any smooth, realistic isotropic potentials where the potentials can be fitted by the multi-SCPPS closure. The multi-SCPPS closure includes the multi-Yukawa closure as a special case. The quasianalytic multi-SCPPS-MSA algorithm can treat realistic fluid mixtures with computational convenience. This makes this method a most appropriate tool for the use of statistical mechanics in practical, engineering applications.

We have demonstrated the power of the algorithm for two binary-component LJ systems: one is composed of particles with nearly the same sizes, but the other with widely different

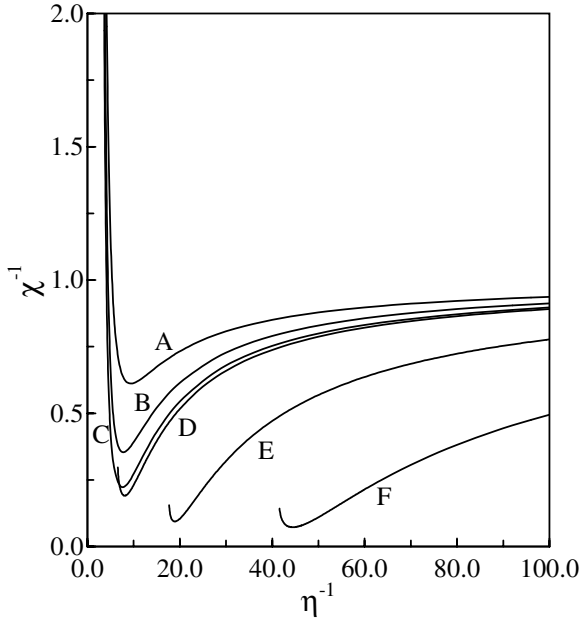

Figure 12. Inverse isothermal compressibility χ^{-1} as a function of η^{-1}. The letters A to F attached to curves have the same meanings as in figure 1.

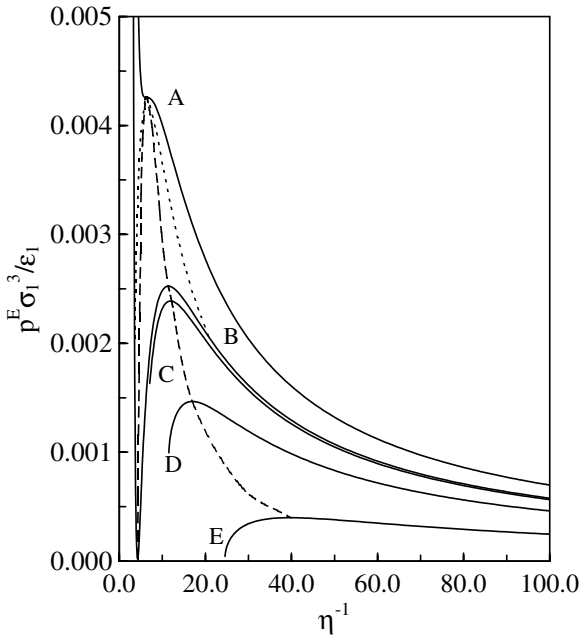

Figure 13. The same as figure 1 but for model 2. The reduced temperatures are $T_A^* = 2.427$, $T_B^* = 2.041$, $T_C^* = 2.0$, $T_D^* = 1.667$ and $T_E^* = 1.0$.

sizes. We have obtained isotherms of the energy pressure p^E and virial pressure p^V in a wide range of temperatures and densities. We have also analysed the thermodynamic states of

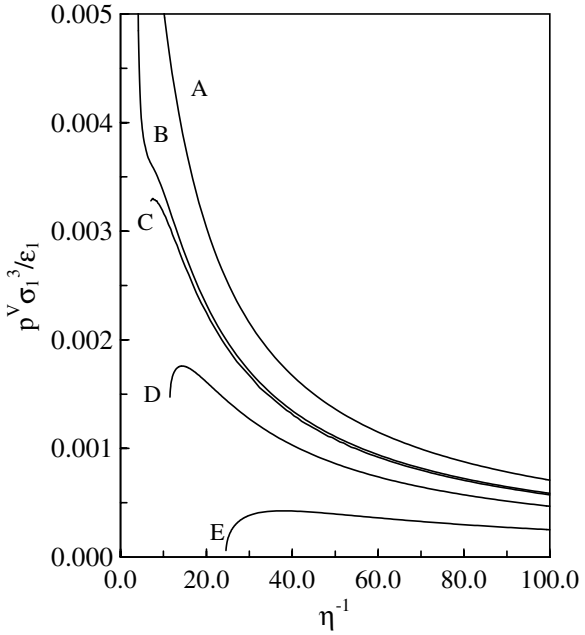

Figure 14. The same as figure 13 but for the virial pressure p^{V}.

the systems along the isotherms from the microscopic standpoints in connection with particle distributions and have shown that the present method is able to detect vapour–liquid transitions and perhaps liquid–glass transitions.

The present approximate method can be further extended: a cluster expansion method, such as the exponential approximation (EXP) [19, 20], can be used to improve the relatively poor MSA RDF. A generalized mean spherical approximation (GMSA) type of approach may further increase the accuracy of the MSA.

This work will be complemented with an evaluation of the MSA results by comparison with corresponding numerical simulation values in a subsequent paper.

Appendix A.

The coefficients A_j, B_j and $\check{C}_{ij}^{(k)}(z_n) = (z_n/2\pi)C_{ij}^{(k)}(z_n)$ in equation (8) are

$$A_j = \frac{2\pi}{\Delta}\left[1 + \frac{1}{2}\zeta_2\beta_j - \sum_{n=1}^{N}\sum_{\tau=-1}^{L}\sum_{l}\rho_l\mathcal{D}_{lj}^{(\tau)}(z_n)\frac{2\pi K_{n_1n_2}^{(n,\tau)}}{z_n}H_{lj}^{(\tau,0)}(z_n)\right], \tag{A.1}$$

$$B_j = \beta_j - \tfrac{1}{2}\sigma_j A_j, \tag{A.2}$$

$$\check{C}_{ij}^{(k)}(z_n) = -\mathcal{D}_{ij}^{(k-1)}(z_n)K_{n_1n_2}^{(n,k-1)} + (k+1)\mathcal{D}_{ij}^{(k)}(z_n)K_{n_1n_2}^{(n,k)} + \sum_{l}\sum_{\tau=1}^{L+2-k} C_{\tau-1}^{\tau+k-1}\mathcal{D}_{lj}^{(\tau+k-2)}(z_n)K_{n_1n_2}^{(n,\tau+k-2)}\exp[\mathcal{G}_{il}^{(\tau)}(z_n)]\frac{2\pi\rho_l \mathrm{e}^{-z_n\sigma_{il}}}{z_n^{3-\tau}}, \tag{A.3}$$

where

$$\beta_j = \frac{\pi}{\Delta}\sigma_j + \frac{2\pi}{\Delta}\sum_{n=1}^{N}\sum_{\tau=-1}^{L}\sum_{l}\rho_l\mathcal{D}_{lj}^{(\tau)}(z_n)\frac{2\pi K_{n_1n_2}^{(n,\tau)}}{z_n}\left[H_{lj}^{(\tau,1)}(z_n) - \frac{1}{2}\sigma_j H_{lj}^{(\tau,0)}(z_n)\right], \tag{A.4}$$

$$H_{lj}^{(\mu,m)}(z_n) = z_n^{\mu+1}[\chi^{(m+\mu+1)}(\lambda_{jl}, z_n) - \Phi_{lj}^{(m+\mu+1,m)}(0, z_n)] + \sum_{k=0}^{\mu+1}\sum_{\xi=0}^{k}\frac{z_n^{k-\xi}k!}{(k-\xi)!}\sum_{\nu}\Phi_{\nu j}^{(m+k-\xi,m)}(0, z_n)C_{\mu+1-k}^{\mu+1}\gamma_{l\nu}^{(\mu+2-k)}(z_n), \tag{A.5}$$

$$\mathrm{e}^{-s\lambda_{jl}}\Phi_{lj}^{(n,m)}(s, z) = \chi^{(n)}(\lambda_{jl}, z+s) - \chi^{(n)}(\sigma_{jl}, z+s) - \sigma_{lj}^{n-m}\mathrm{e}^{-z\sigma_{lj}}[\chi^{(m)}(\lambda_{jl}, s) - \chi^{(m)}(\sigma_{jl}, s)], \tag{A.6}$$

$$\chi^{(k)}(b, a) = \int_b^\infty \mathrm{d}r\, r^k\mathrm{e}^{-ar} = k!\mathrm{e}^{-ab}\sum_{\xi=0}^{k}\frac{b^{k-\xi}}{a^{\xi+1}(k-\xi)!} \qquad (b \neq 0), \tag{A.7}$$

and

$$\chi^{(k)}(0, x+\mathrm{i}y) = \frac{k!}{(x^2+y^2)^{(k+1)/2}}\left\{\cos\left[(k+1)\tan^{-1}\frac{y}{x}\right] - \mathrm{i}\sin\left[(k+1)\tan^{-1}\frac{y}{x}\right]\right\}. \tag{A.8}$$

Also, $\zeta_k = \sum_l \rho_l\sigma_l^k$, $\Delta = 1 - \pi\zeta_3/6$, $C_m^n = n!/m!(n-m)!$ and $K_{n_1n_2}^{(n,\tau)}$ are normalization constants. The unknowns $\mathcal{D}_{il}^{(m)}(z_n)$ and $\mathcal{G}_{ij}^{(m)}(z_k)$ are

$$\mathcal{D}_{il}^{(m)}(z_n) = \frac{z_n D_{il}^{(m)}(z_n)}{2\pi K_{n_1n_2}^{(n,m)}}, \qquad \mathcal{G}_{ij}^{(m)}(z_k) = \ln\left[\frac{\gamma_{ij}^{(m)}(z_k)z_k^{3-m}\mathrm{e}^{z_k\sigma_{ij}}}{2\pi\rho_j}\right], \tag{A.9}$$

where

$$s^{2-m}\gamma_{il}^{(m)}(s) = 2\pi\rho_l\tilde{g}_{il}^{(m)}(s) = 2\pi\rho_l\int_{\sigma_{il}}^\infty \mathrm{d}x\,\mathrm{e}^{-sx}x^m g_{il}(x). \tag{A.10}$$

Appendix B.

The coefficients $\breve{A}_{ij}^{(m)}(z_k)$, $\breve{B}_{ij}^{(m)}(z_k)$, $\breve{C}_{ilj}^{(m,\tau)}(z_k, z_n)$ and $\breve{D}_{ilj}^{(m,\tau)}(z_k, z_n)$ in equation (9) and functions $\tilde{Q}_{lj}^{(m)}(\mathrm{i}s)$ in equation (10) are

$$\breve{A}_{ij}^{(m)}(z_k) = \frac{z_k\mathrm{e}^{z_k\sigma_{ij}}}{2\pi}\chi^{(m+1)}(\sigma_{ij}, z_k) + \tfrac{1}{2}\sum_l\rho_l\sum_{\xi=0}^{m}\exp[\mathcal{G}_{il}^{(\xi+1)}(z_k)]C_\xi^m\Phi_{lj}^{(m-\xi+2,m-\xi)}(z_k, 0), \tag{B.1}$$

$$\breve{B}_{ij}^{(m)}(z_k) = \frac{z_k\mathrm{e}^{z_k\sigma_{ij}}}{2\pi}\chi^{(m)}(\sigma_{ij}, z_k) + \sum_l\rho_l\sum_{\xi=0}^{m}\exp[\mathcal{G}_{il}^{(\xi+1)}(z_k)]C_\xi^m\Phi_{lj}^{(m-\xi+1,m-\xi)}(z_k, 0), \tag{B.2}$$

$$\breve{C}_{ilj}^{(m,\tau)}(z_k, z_n) = -\delta_{il}z_n^\tau z_k\mathrm{e}^{z_k\sigma_{lj}}\chi^{(m+\tau)}(\sigma_{lj}, z_n+z_k) + \frac{2\pi}{z_n}\rho_l\tau!\sum_{\xi=0}^{m}\exp[\mathcal{G}_{il}^{(\xi+1)}(z_k)]C_\xi^m\sum_{\eta=0}^{\tau}\frac{z_n^{\tau-\eta}}{(\tau-\eta)!}\Phi_{lj}^{(m-\xi+\tau-\eta,m-\xi)}(z_k, z_n), \tag{B.3}$$

$$\breve{D}_{ilj}^{(m,\tau)}(z_k, z_n) = 2\pi z_n^\tau\rho_l\sum_{\xi=0}^{m}\exp[\mathcal{G}_{il}^{(\xi+1)}(z_k)]C_\xi^m\mathrm{e}^{z_k\lambda_{jl}}\chi^{(m-\xi+\tau+1)}(\lambda_{jl}, z_n+z_k), \tag{B.4}$$

and

$$\mathrm{e}^{-s\lambda_{lj}}\tilde{Q}_{lj}^{(m)}(\mathrm{i}s) = \tfrac{1}{2}A_j\Phi_{lj}^{(m+2,m)}(s, 0) + B_j\Phi_{lj}^{(m+1,m)}(s, 0) + \sum_{n=1}^{N}\sum_{k=0}^{L+1}\sum_{\xi=0}^{k}\frac{z_n^{k-\xi}C_{lj}^{(k)}(z_n)k!}{(k-\xi)!}\Phi_{lj}^{(m+k-\xi,m)}(s, z_n)$$

$$+\sum_{n=1}^{N}\sum_{\tau=-1}^{L} D_{lj}^{(\tau)}(z_n) z_n^{\tau+1} \mathrm{e}^{-s\lambda_{lj}} \chi^{(m+\tau+1)}(\lambda_{jl}, z_n + s). \tag{B.5}$$

Appendix C.

The quantities $[\tau\gamma_{ij}^{(\tau+2)}(z_n) - \gamma_{ij}^{(\tau+3)}(z_n)]$ for $(-1 \leqslant \tau \leqslant L)$ in equation (37) are given by

$$\tau\gamma_{ij}^{(\tau+2)}(z_n) - \gamma_{ij}^{(\tau+3)}(z_n) = \sqrt{\frac{c_j}{c_i}} z_n^{\tau+1}[(\tau+1)\{\hat{\Gamma}^{(\tau+2)}(z_n)\}_{ij} + z_n\{\hat{\Gamma}'^{(\tau+2)}(z_n)\}_{ij}], \tag{C.1}$$

where the derivatives $\{\hat{\Gamma}'^{(\tau+2)}(z_n)\}_{ij}$ are given by the following asymptotic relations:

$$\{\hat{\Gamma}'^{(1)}(s)\}_{ij} = \sum_l \Bigg[-\frac{\{\hat{\Lambda}^{(0)}(s)\}_{il}}{s} - \{\hat{\Lambda}^{(1)}(s)\}_{il} - \sum_k \{\hat{\Gamma}^{(1)}(s)\}_{ik} (\rho_k\rho_l)^{1/2} \tilde{Q}_{kl}^{(1)}(\mathrm{i}s) \Bigg] \{\hat{Q}^{(0,0)}(\mathrm{i}s)^{-1}\}_{lj} \tag{C.2}$$

and

$$\begin{aligned}\{\hat{\Gamma}'^{(m+1)}(s)\}_{ij} = \sum_l \Bigg[& -\frac{\{\hat{\Lambda}^{(m)}(s)\}_{il}}{s} - \{\hat{\Lambda}^{(m+1)}(s)\}_{il} \\ & - \sum_{\xi=0}^{m}\sum_k \{\hat{\Gamma}^{(\xi+1)}(s)\}_{ik} C_\xi^m (\rho_k\rho_l)^{1/2} \tilde{Q}_{kl}^{(m+1-\xi)}(\mathrm{i}s) \\ & - \sum_{\xi=0}^{m-1}\sum_k \{\hat{\Gamma}'^{(\xi+1)}(s)\}_{ik} \{\hat{Q}^{(m,\xi)}(\mathrm{i}s)\}_{kl} \Bigg] \{\hat{Q}^{(m,m)}(\mathrm{i}s)^{-1}\}_{lj},\end{aligned} \tag{C.3}$$

where

$$\begin{aligned}\{\hat{\Lambda}^{(m)}(s)\}_{ij} = \frac{(\rho_i\rho_j)^{1/2}}{s} \Bigg\{ & A_j \chi^{(m+1)}(\sigma_{ij}, s) + B_j \chi^{(m)}(\sigma_{ij}, s) \\ & - \sum_n \sum_{\tau=0}^{L+1} z_n^{\tau+1} C_{ij}^{(\tau)}(z_n) \chi^{(m+\tau)}(\sigma_{ij}, z_n + s) \Bigg\}\end{aligned} \tag{C.4}$$

and

$$\{\hat{Q}^{(m,\xi)}(\mathrm{i}s)\}_{lj} \equiv \delta_{lj}\delta_{m\xi} - C_\xi^m (\rho_l\rho_j)^{1/2} \tilde{Q}_{lj}^{(m-\xi)}(\mathrm{i}s). \tag{C.5}$$

References

[1] Yasutomi M 2001 *J. Phys.: Condens. Matter* **13** L255
[2] Yasutomi M 2002 *J. Phys.: Condens. Matter* **14** L165
[3] Yasutomi M 2002 *J. Phys.: Condens. Matter* **14** L435
[4] Blum L and Høye J S 1978 *J. Stat. Phys.* **19** 317
[5] Giunta G, Abramo M C and Caccamo C 1985 *Mol. Phys.* **56** 319
[6] Arrieta E, Jedrzejek C and Marsh K N 1987 *J. Chem. Phys.* **86** 3607
[7] Arrieta E, Jedrzejek C and Marsh K N 1991 *J. Chem. Phys.* **95** 6806
[8] Henderson D, Waisman E, Lebowitz J L and Blum L 1978 *Mol. Phys.* **35** 241
[9] Stell G and Weis J J 1980 *Phys. Rev.* A **21** 645
[10] Konior J and Jedrzejek C 1988 *Mol. Phys.* **63** 655
[11] Henderson D, Waisman E, Lebowitz J L and Blum L 1978 *Mol. Phys.* **35** 241
[12] Høye J S and Stell G 1977 *J. Chem. Phys.* **67** 439
[13] William H P, Brian P F, Saul A T and William T V 1988 *Numerical Recipes in C* (Cambridge: Cambridge University Press)

[14] Landau L D and Lifshitz E M 1958 *Statistical Physics* (London: Pergamon)
[15] Huang K 1963 *Statistical Mechanics* (New York: Wiley)
[16] Hansen J P and McDonald I R 1976 *Theory of Simple Liquids* (London: Academic)
[17] Hansen J P and Verlet L 1969 *Phys. Rev.* **184** 151
[18] Sarkisov G 2001 *J. Chem. Phys.* **114** 9496
[19] Anderson H C, Chandler D and Weeks J D 1976 Roles of repulsive and attractive forces in liquids: the equilibrium theory of classical fluids *Adv. Chem. Phys.* **34** 105
[20] Stell G 1976 Fluids with long-range forces: toward a simple analytic theory *Phase Transition and Critical Phenomena* vol 15, ed C Domb and M S Green (London: Academic) p 47